Calibration of the Marshall Grazing Incidence X-Ray Spectrometer Experiment. II. Flight Instrument Calibration

P. S. Athiray[1] , Amy R. Winebarger[2] , Patrick Champey[2] , Ken Kobayashi[2] , Sabrina Savage[2] , Brent Beabout[2], Dyana Beabout[2], David Broadway[2], Alexander R. Bruccoleri[3] , Peter Cheimets[4], Leon Golub[4] , Eric Gullikson[5], Harlan Haight[2], Ralf K. Heilmann[6] , Edward Hertz[4], William Hogue[2], Steven Johnson[2], Jeffrey Kegley[2], Jeffery Kolodziejczak[2], Chad Madsen[4] , Mark L. Schattenburg[6] , Richard Siler[2], Genevieve D. Vigil[2] , and Ernest Wright[2]

[1] NASA Postdoctoral Program, NASA Marshall Space Flight Center, ST13, Huntsville, AL, USA; athiray.panchap@nasa.gov
[2] NASA Marshall Space Flight Center, Huntsville, AL 35812, USA
[3] Izentis LLC, PO Box 397002, Cambridge, MA 02139, USA
[4] Center for Astrophysics | Harvard & Smithsonian, 60 Garden Street, Cambridge, MA 02138, USA
[5] Center for X-Ray Optics, Lawrence Berkeley National Laboratory, Berkeley, CA 94720, USA
[6] Space Nanotechnology Laboratory, MIT Kavli Institute for Astrophysics and Space Research, Massachusetts Institute of Technology, Cambridge, MA 02139, USA

Abstract

The Marshall Grazing Incidence X-ray Spectrometer (MaGIXS) is a sounding rocket experiment that observes the soft X-ray spectrum of the Sun from 6.0–24 Å (0.5–2.0 keV), successfully launched on 2021 July 30. End-to-end alignment of the flight instrument and calibration experiments are carried out using the X-ray and Cryogenic Facility at NASA Marshall Space Flight Center. In this paper, we present the calibration experiments of MaGIXS, which include wavelength calibration, measurement of line spread function, and determination of effective area. Finally, we use the measured instrument response function to predict the expected count rates for MaGIXS flight observation looking at a typical solar active region.

1. Introduction

Understanding what drives the physics of coronal heating remains one of the critical problems of solar physics. Though many different theories have been put forth (e.g., Cranmer & Winebarger 2019), two of the most likely competing physical mechanisms are sporadic energy release through magnetic reconnection (Parker 1988; Cargill et al. 1995; Klimchuk 2006) and steadier energy release through dissipation of Alfvén waves (e.g., Asgari-Targhi & van Ballegooijen 2012). One of the fundamental differences between these mechanisms is the frequency of heating events ($1/\tau_{heat}$), where τ_{heat} is the average time between two heating events on a loop strand. The evolution of the plasma temperature and density depend strongly on τ_{heat}. For high-frequency heating, where the time between heating events is much shorter than the cooling time of the plasma, the temperature and density remain relatively constant, while for low-frequency heating, where the time between heating events is long compared to the cooling time, they evolve dynamically. For cases where loop strands are not resolved, different heating scenarios result in different predicted distributions of the temperature of the plasma. A proxy for the distribution of the plasma temperature is called the differential emission measure (DEM) distribution, or its integral form, emission measure (EM) distribution, which would be an observational discriminator to distinguish the mechanisms. A broad DEM with the presence of higher than average coronal temperatures would imply low-frequency heating, while high-frequency heating would yield a narrow DEM (Klimchuk 2017). Measuring the high-temperature EM slope is found to be the *smoking gun* observation required to constrain the timescale of heating events (e.g., Barnes et al. 2016a, 2016b, 2019; Reep et al. 2013). Although some limited diagnostics are currently available to discriminate high-temperature emission (e.g., Warren et al. 2012), most current space

instrumentation has a so-called *blindspot* to the crucial low EM, high-temperature plasma above 5 MK (Winebarger et al. 2012). Athiray et al. (2019) demonstrated that the ratios of emission lines from Fe XVII, XVIII, and XIX are particularly sensitive to the high-temperature EM slope and provide an excellent diagnostic of coronal heating frequencies.

The Marshall Grazing Incidence X-ray Spectrometer (MaGIXS) is a sounding rocket experiment developed by the NASA Marshall Space Flight Center (MSFC) and the Smithsonian Astrophysical Observatory (SAO), launched successfully on 2021 July 30 from the White Sands Missile Range, NM. MaGIXS is designed to observe, for the first time, soft X-ray emission of high-temperature, low-emission plasma of spatially and spectrally resolved solar coronal structures in the energy range from 0.5–2.0 keV (Kobayashi et al. 2010, 2018; Champey et al. 2016). The MaGIXS spectrometer is sensitive to a series of warm and hot plasma emission lines simultaneously through the same optical path, providing spatial information along a slot. The bandpass includes several emission lines formed by the key ionization stages of Fe (XVII, XVIII, and XIX), which will extend the DEM coverage from 3–10 MK and thereby help to constrain the slope of the high-temperature EM falloff (e.g., Athiray et al. 2019).

Because the determination of the high-temperature falloff requires ratios of spectral lines formed at different wavelengths, knowledge of the relative calibration and potential errors in calibration are required. We were particularly motivated to constrain the radiometric calibration in the 10–17 Å region, which contains several of these important diagnostic lines. Therefore, we have performed a detailed characterization of MaGIXS using targets that emit X-ray lines in the above wavelength range, at the NASA MSFC X-ray and Cryogenic Facility (XRCF). Prior to calibration tests, we established an
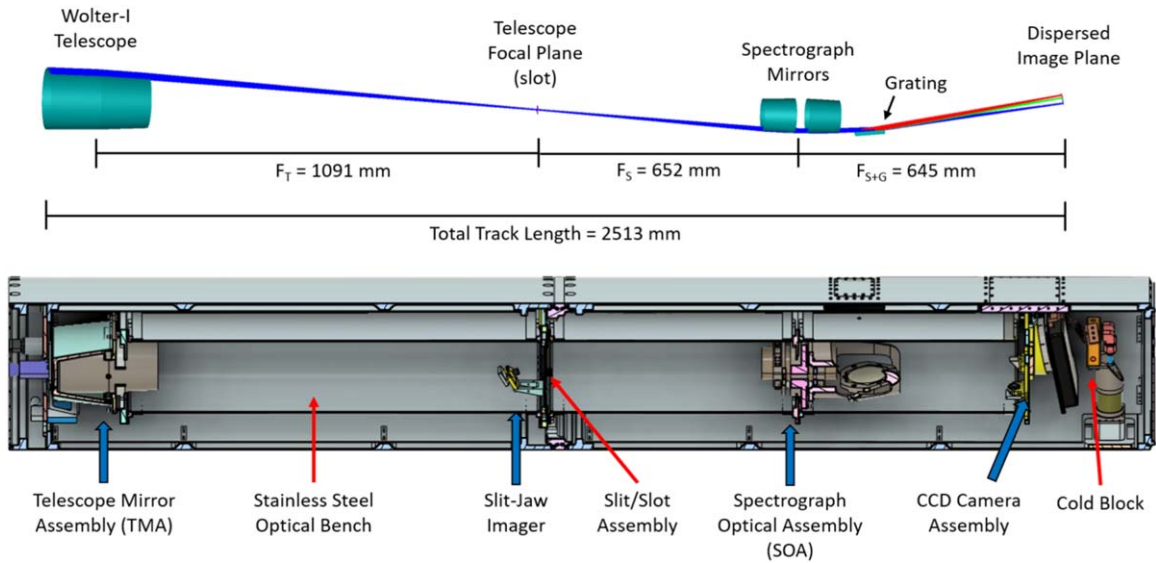
Figure 1. The optical layout and ray trace of the MaGIXS instrument design. All the major optical components, excluding the slit-jaw imaging system, filters, and science camera are listed in the figure.

optimized method for photon counting in CCD images, and applied the same to characterize the X-ray source at XRCF, which is used for MaGIXS calibration. These results are published in Athiray et al. (2020), hereafter referred to as Paper I.

In this paper, we present the experiments, analysis, and results of the ground calibration of MaGIXS carried out at the XRCF. Section 2 provides a description of the MaGIXS instrument design, a brief overview of the optical components, and a short summary of the alignment and testing of the X-ray mirrors. In Section 3, we describe the calibration experiment test setup and provide a summary of data collection. Methods of data analysis and results including wavelength calibration, point-spread function (PSF), estimation of throughput flux, and determination of effective area of MaGIXS are detailed in Section 4. In Section 5, we describe the predicted expected count rates from the MaGIXS flight for a typical active region using the calibration products, and we conclude with an overall summary and discussion in Section 6.

2. MaGIXS Instrument Overview

2.1. Instrument Description

The MaGIXS optical instrument is described in detail in Kobayashi et al. (2014) and Champey et al. (2015) and reviewed briefly here. The instrument includes a single shell Wolter-I type telescope mirror, a slot with slit-jaw context imager, a pair of conjugate parabolic spectrometer mirrors (SM1 and SM2), a grating, and a CCD detector. The design also includes several small reference mirrors and alignment reticles, which are used for co-alignment of optical elements. Figure 1 shows the optical layout of MaGIXS with all the key optical components distinctly marked. The top panel in Figure 1 shows the optical path in X-rays. Table 1 summarizes the specifications of the individual optical components of MaGIXS.

MaGIXS is the first instrument to fly X-ray mirrors that were polished using a state-of-the-art deterministic polishing technique, which was shown to significantly minimize figure errors of the mandrels (Davis et al. 2019; Champey et al. 2019).

Because only a segment of each of the reflective surfaces (see ray trace Figure 1) directs rays to the grating, deterministic polishing only occurred over a 43° section of each mandrel. The 73 mm long, varied line space, planar diffraction grating, fabricated by Izentis LLC, diffracts $\approx 34°$ of the full system aperture, dispersing primarily the first order diffracted X-ray beam and second order beam to the science camera. The X-ray mirrors, including a telescope and spectrometer (SM1 and SM2), and grating are mounted on appropriate structures to form different assembly modules, which was carried out at SAO. The telescope mirror assembly (TMA) carries the Wolter-I optic, and the arrangement of spectrometer mirrors aligned to the grating is collectively called the spectrometer optical assembly (SOA). A thorough description of the assemblies (TMA, SOA) along with the adopted alignment methods are presented in Hertz et al. (2020).

The science camera has been developed by MSFC for suborbital missions (Rachmeler et al. 2019) and utilizes a back-illuminated, ultra-thinned, astro-processed Te2V CCD. The camera is positioned off-axis to collect chiefly the first-order diffracted spectral image. In addition to the X-ray optical system, MaGIXS also includes a slit-jaw context imager to aid in pointing during flight and alignment to other data sets after flight. The slit-jaw system provides context solar image during the flight.

Finally, the MaGIXS instrument includes an entrance and focal plane filter. The entrance filter is 50 nm of Al mounted on mesh, while the focal plane filter is 150 nm of Al mounted on polyimide. The entrance filter was chosen to allow for EUV light to be focused at the focal plane of the TMA and reimaged by the slit-jaw optics, while the focal plane filter was chosen to reduce the out of band light on the detector. For purposes of the effective area calculation, we assume the surfaces of the filters have oxidized and include a 10 nm thickness of Al_2O_3.

2.2. Instrument Configurations

For the end-to-end alignment and calibration tests, MaGIXS was built sequentially from the telescope end to the science camera end, adding each optical component one-by-one in the

Table 1
Summary of Description of MaGIXS Optical Components

S.No	Optical Component		Description	Remarks
	TMA	Entrance filter	50 nm of Al with (assumed) 10 nm of Al_2O_3 mounted on 70 lpi Ni mesh	Test configuration: No filter
				Flight configuration: Filter present
		Telescope mirror	Mirror type: Wolter-I, Ni replicated	Test configuration: Spacers for source at finite distance
			Graze angle: 1°	
			Surface roughness: 0.5 nm	Flight configuration: Spacers for source at infinity
			Focal length: 1.09 m	
			Geometric area (A_{geo}): 0.87 cm^2	
			Coating: Iridium, 40 nm thick	
2	Slot		Molybdenum film on circular aluminum mount, 3.84 mm wide, 10.5 mm long	Test configuration: Custom slot with large pinholes (see Figure 2, text)
			Circular aluminum mount, 25 mm diameter	Flight configuration: 12′ wide, 33′ long
3	SOA	Spectrometer mirrors, SM1 and SM2	Mirror type: Paraboloid Ni replicated	
			Graze angle: 2 °	
			Surface roughness: 0.5 nm	
			Focal length: 0.79 m	
			Coating: Iridium, 40 nm thick	
			Graze angle: 2°	
		Grating	Blaze angle: 1.6°	Efficiency measured at LBNL
			Coating: Iridium, 5 nm thick, 73 mm long	
			Varied line spacing (d_{center}: 4760 Å)	
4	Focal plane filter		150 nm Al with (assumed) 10 nm Al_2O_3 mounted on 200 nm polyimide	
5	Detector		CCD 2×1 k pixels, 15 μm pixel size	

Table 2
Summary of Test Series and Instrument Arrangement

S.No	Test Series	Instrument Setup	Remarks
1	TMA focus check	Source: TMA camera	Series of experiments to evaluate On-/Off-axis TMA performance
2	Alignment check	Source: TMA-slot–SM1-SM2 camera	Series of experiments at out-of-focus positions to verify alignment
3	Calibration	Source: TMA-slot-SOA camera	Observed a shift in the SOA position during the first round of calibration experiments, adjusted the SOA position performed in the final calibration described in this paper

test configuration, which is slightly different from the *flight configuration*. We highlight the differences between the two configurations in the remarks column in Table 1. After adding each component, the built-up instrument was aligned using a theodolite and reference mirrors and reticles, and confirmed by X-ray measurements at the XRCF, which is a 500 m evacuated X-ray beamline. The assembly tests were designed to confirm the focal position of the TMA and to verify the alignment of the overall integrated instrument. Table 2 gives a broad overview of the test series performed at XRCF and the corresponding instrument setup. A paper summarizing the alignment strategy employed for MaGIXS will be presented elsewhere (P. Champey et al. 2021, in preparation). These alignment checks also provide data we can use for component level calibration of the X-ray mirrors, discussed in Section 4.6.2. Additionally, before integration into the SOA, the grating was tested independently at the Lawrence Berkeley National Laboratory (LBNL). The results of that test are also given in Section 4.6.2.

MaGIXS was originally designed with a narrow slit at the focus position of the TMA. Soon after we conducted X-ray alignment tests with the TMA, we realized that it was difficult to co-align the instrument with the original slit that was aimed to achieve 6″ angular resolution. However, due to the degraded mirror PSF and the advancement of unfolding techniques for slot imaging spectrograph data (Winebarger et al. 2019), it was determined to replace the slit with a 12′ slot during integration and calibration. For the test configuration, we fabricated a custom-made slot with three large pinholes drilled on an Al slit each ∼1 mm in size, one at the center of the slot (on-axis) and two on either side of the center of the slot (off-axis) as shown in Figure 2. The off-axis pinholes are spaced about 9.5′ from the center hole. For the flight configuration, the custom designed pinhole slot will be replaced with a newly fabricated lumogen coated slot mask ∼3.84 mm, i.e., ∼12′ wide and 33′ long. We mention that results of MaGIXS calibration in the test configuration can be applied to the flight configuration, as
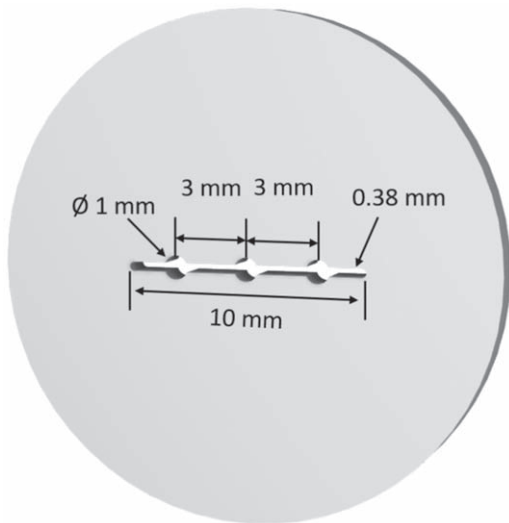
Figure 2. Sketch of the custom slot made with three large pinholes used for the calibration tests.

changes are minimal (see Table 1, Columns 4 and 5) and does not affect the calibration parameters.

3. MaGIXS Calibration

The goal of MaGIXS calibration is to determine the wavelength calibration, assess the line-spread function (LSF) and PSF, and measure the actual effective area of the instrument. In this section, we describe the calibration experimental setup, the sources used, and the summary of data collected.

3.1. Experiment Setup

Figure 3 shows a schematic of the MaGIXS calibration setup assembled in the test configuration at the XRCF. The aligned, built-up instrument (TMA-slot-SOA camera) is placed on the five axis mount stage on the experiment station inside the XRCF vacuum chamber. The entrance of the TMA is placed at a distance of ≈536 m from the X-ray source. The X-rays from the source are transmitted through an evacuated 518 m long guide tube to an evacuated 7.3 m diameter × 22.9 m long instrument chamber. An optical laser is also placed at the source end next to the X-ray source, which is used to provide a rough alignment between the source and the telescope in air. This laser could be seen on the slot surface at the focus of the TMA using the slit-jaw imager. The flight camera is placed at the off-axis detector plane to measure the wavelength dispersed image coming from the grating. The CCD is mounted in a copper carrier that is connected via a copper strap to a cold block. The cold block is actively cooled to roughly −100°C using liquid nitrogen, which results in a CCD carrier average temperature of roughly −70°C. The carrier temperature is controlled such that it is maintained constant within ±5°C. During one of our calibration test runs the cooling system was paused inadvertently and resulted in increased noise in the CCD, which is described in Section 3.3.

The facility provided a beam normalization detector (BND) to monitor the incident X-ray spectrum and flux. The BND is a flow proportional counter (FPC) that uses flowing P10 gas (90% argon, 10% methane) at a pressure of 400 Torr. For a detailed description of the FPC, see Wargelin et al. (1997). The

BND is mounted on a translation stage within the guide tube at a distance of 38 m from the source, and outside of the Electron Impact Point Source-CCD beam path. Apertures of appropriate diameters are used in front of the BND to avoid saturation. In Paper I, we established that the flux measured from the BND is reliable to within 20% and is consistent with the values reported in literature. We employed the same BND to simultaneously monitor the incident flux during the end-to-end alignment tests as well as for the calibration tests.

3.2. X-Ray Source

For calibration tests, the X-ray source at XRCF was operated with an anode voltage that is 4 × the L-shell or 5 × the K-shell binding potential of the target at a permissible current. A list of the targets, used for the end-to-end alignment tests and calibration tests is given in Table 3. No filter was placed in front of the X-ray source for the calibration tests. The unfiltered X-ray source spectrum comprises target lines and bremsstrahlung continuum. The X-ray source operating parameters such as anode voltage and current (Columns 4 and 5) are chosen such that the expected photon flux on CCD is relatively low to perform *photon counting* and also to avoid saturation and pileup of artifacts in the resulting image.

3.3. Data Summary and Preprocessing

The converged X-ray beam from the TMA was allowed to pass through the pinhole slot at three different positions along the slot viz on-axis S0 (center), and off-axis S1, S2 (either side of the slot center), respectively. Calibration data were acquired for different targets using the science camera operated in the frame transfer mode with an exposure time of ∼3 s per frame. More than 600 frames of data were acquired at each beam position for adequate statistics. Data for the Zn target was collected only at the S0 position due to limited beam time availability. Dark frames were acquired at regular intervals by closing a gate valve between the source and the MaGIXS telescope. Standard CCD data reduction routines are followed to remove bias level, dark current, and fixed pattern noise in the images. The measured gain of the camera was determined prior to calibration tests using a sealed radioactive source Fe^{55} and found to be ∼2.66 electrons per data number. The measured rms read noise is approximately 10 e, which includes read and dark noise. The camera cooling was inadvertently halted during the measurement of data set #3 in Table 3. The subsequent rise in temperature introduced additional dark noise and hot pixels to that data set. Extra care was taken while processing the data to isolate hot pixels. We note the data set is still useful for wavelength calibration, however the additional noise complicates the ability to precisely determine the photon energy and hence has limited usefulness for radiometric calibration. Figure 4 shows a summary of collated, uncalibrated, pre-processed MaGIXS data collected from the calibration tests, with the prominent target emission lines and beam positions labeled. This image is a combination of data collected at each target and beam position on the slot, smoothed over 3 pixels for better visualization.

4. Data Analysis

The calibration data are analyzed using the optimized event selection algorithm described in Paper I, which identifies individual photon hit locations and calculates the total energy
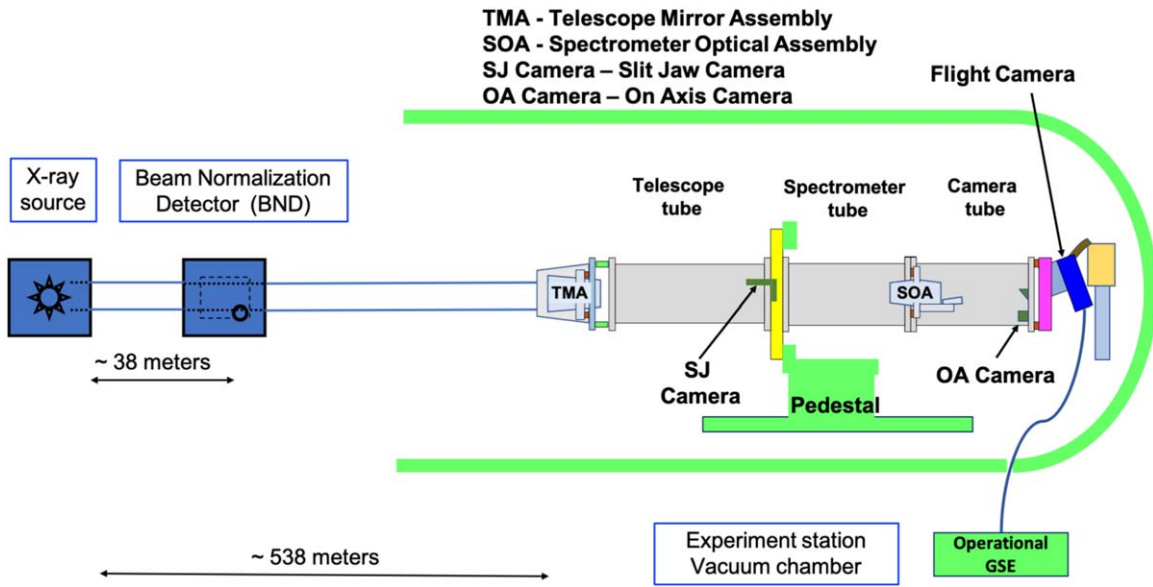
Figure 3. Schematic view of the test setup for MaGIXS calibration tests at XRCF at NASA MSFC. In all test configurations the incident source flux is monitored by a beam normalization detector (BND).

Table 3
List of Calibration Targets and Respective Line Energies

S.No	Target	Line Energy keV	Voltage kV	Current mA	BND Aperture Diameter cm	Test	Source Filter
1	Ni-L	0.85	3.40	5.8	0.1	Calibration	No filter
2	Zn-L	1.01	4.00	3.0	0.1	Calibration	No filter
3	Mg-K[a]	1.25	6.50	1.5	0.1	Calibration	No filter
4	Mg-K	1.25	2.60	3.0	0.4	End-to-end—TMA focus check	K2
5	Mg-K	1.25	2.60	3.0	0.4	End-to-end—alignment check	K2

Note.
[a] This data set contained additional noise.

deposited by each photon on the detector. In the case of multi-pixel events, the algorithm sums adjacent shared pixels to reconstruct the photon energy, and the pixel where the maximum energy is deposited is considered for image construction. Figure 4 was constructed using this algorithm. The MaGIXS is a spectrograph with a diffraction grating, which means photons with different energies (wavelengths) are dispersed and then detected at different pixel coordinates along the dispersion axis on the CCD. Hence, we can measure photon energy in two ways: (i) energy deposited on the detector from a photon event recovered from the event selection algorithm and (ii) the location where photon falls on the detector in the dispersion direction "X," which can be determined through pixel-to-wavelength calibration.

4.1. Calculating Slot-SOA-camera Roll

Using the event processed X-ray images, for each target/pointing data combination, we created summed spectra along the dispersion axis (X) and along the cross-dispersion axis (Y). These summed spectra are fitted with Gaussian functions to determine the mean (X,Y) pixel locations where the peak of the distribution occurs. We find the peaks in X are well aligned at each target line, for different pointing S0, S1 and S2. This alignment implies that we do not find any roll in the slot orientation with respect to the SOA and camera. However, the

locations of the peaks in Y showed a small deviation from parallel to the detector pixel rows at each pointing. This misalignment indicates that there is a small roll angle involved between the SOA and camera, which we determined to be $-0.64°$ from the detector X-axis. For example, Figure 5 shows the uncorrected S0 image plotted on the top panel and the roll angle corrected S0 image plotted in the bottom panel. With this correction, we note how well the spots align with the dispersion (X) axis of the detector indicated by the solid horizontal line. All event processed data are first corrected for this roll angle before the analysis for calibration.
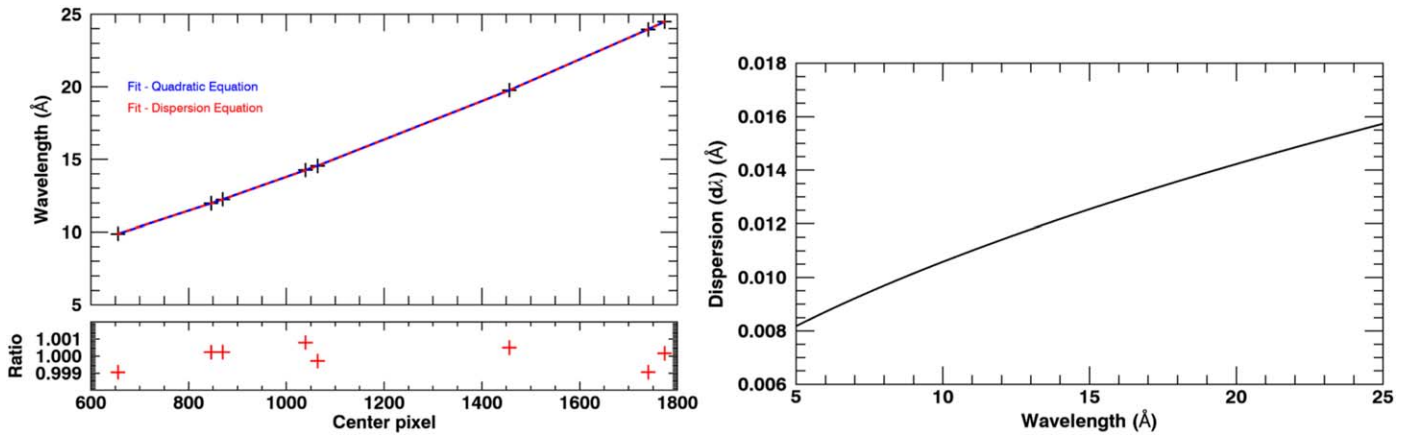
4.2. Wavelength Calibration

The grating disperses convergent X-rays into respective first and second order spectra, which are distinctly observed at different abscissa pixel locations on the detector. The wavelength calibration defines a relationship between the wavelength of the dispersed photon and the most probable pixel location on the detector. The center pixel of the X-ray lines in the observed data was found by fitting a Gaussian curve to each spectral line. Eight wavelengths from three targets, including the first and second orders lines, listed in Table 4 are used for wavelength calibration. First, we have performed an empirical fit to the wavelength calibration using a second order polynomial, which is shown in Figure 6 (left) as a blue line for
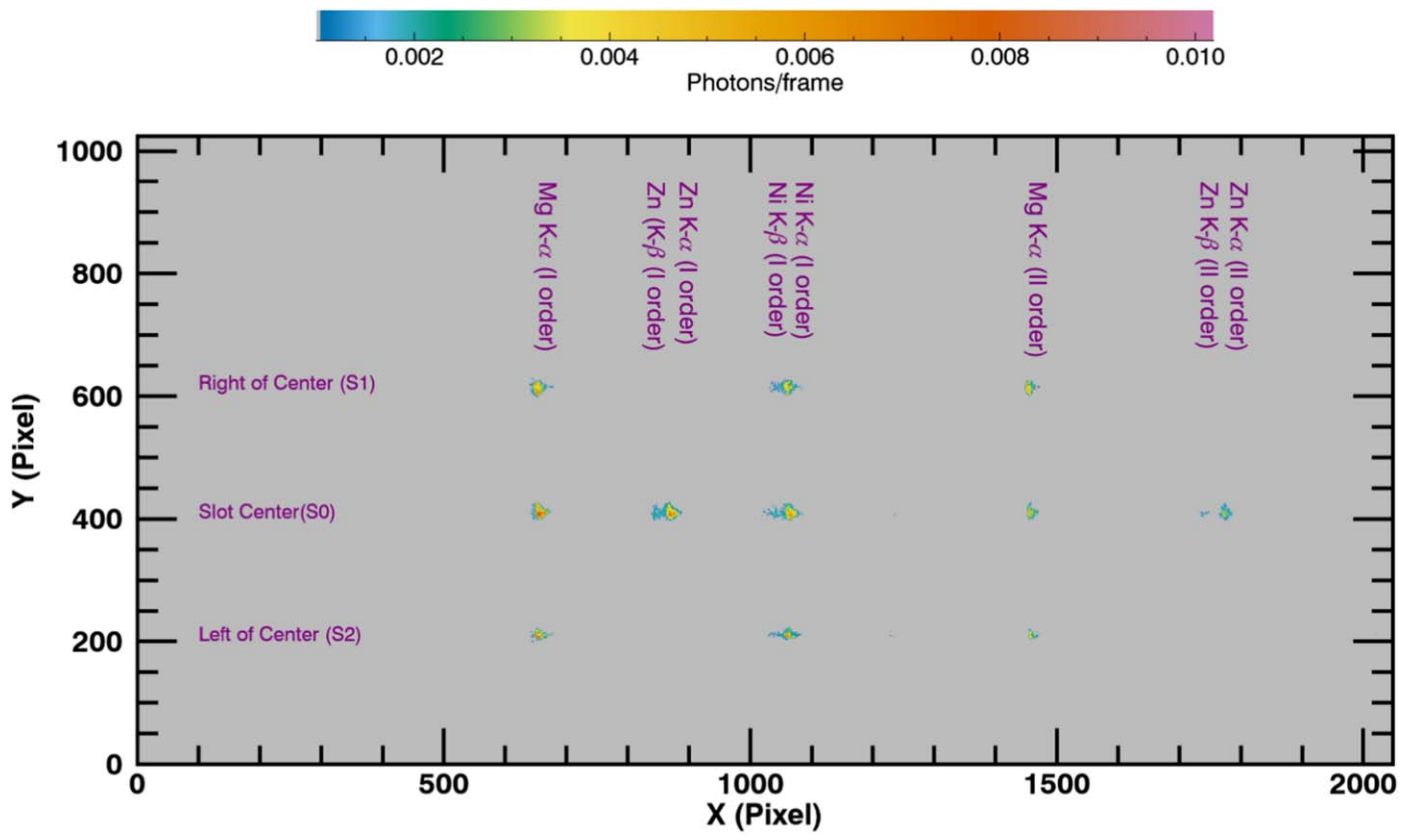
Figure 4. MaGIXS X-ray image summarizing all data collected from the calibration tests normalized with number of data frames at each target and slot position. This image is smoothed over 3 pixels for better data visualization. The data collection includes measurements at three beam positions, S0, S1, and S2, using three targets Mg, Zn, and Ni, respectively, which are labeled. The second orders are dispersed toward the right side of the figure. The data have been event processed, which includes determining photon energy deposits and corresponding photon hit locations to correctly include multi-pixel photon hits.
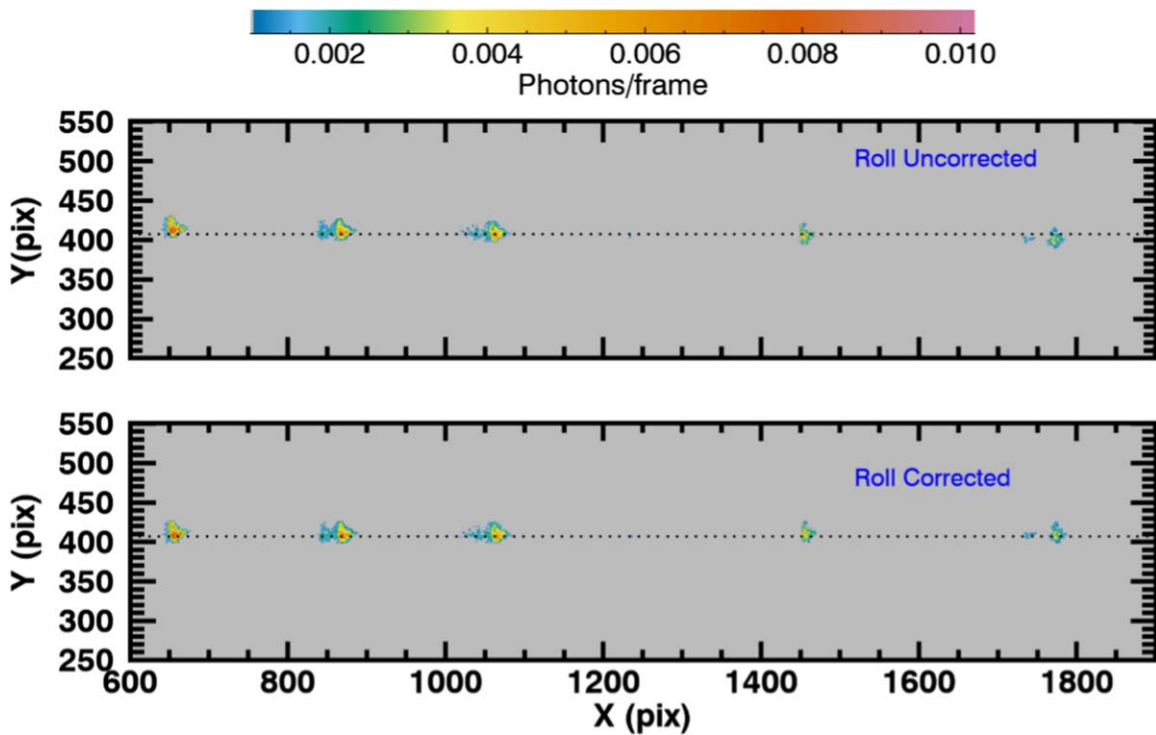
Figure 5. An example plot comparing the cropped S0 image for all targets with and without roll correction applied to the data.

Figure 6. (Left) Wavelength calibration of MaGIXS using eight X-ray lines from three targets including first and second order spectra modeled using a quadratic equation and grating dispersion equation. The bottom panel shows the measure of goodness of the model fit by taking the ratio of calibration wavelength to the modeled wavelength. (Right) Dispersion of MaGIXS grating showing the spectral plate scale.

Table 4
List of Target Lines and Respective Wavelengths from the First and Second Order Diffraction used for MaGIXS Calibration

| S.No | Target Line | Calibration Wavelengths at Different Diffraction Orders | |
		First Order (Å)	Second Order (Å)
1	Mg-K-α	9.88	19.77
2	Zn-L-β	11.97	23.95
3	Zn-L-α	12.25	24.50
4	Ni-L-β	14.26	
5	Ni-L-α	14.55	

the on-axis S0 position. This fit will be applied to the flight data for scientific analysis. Similar empirical fits are performed for the S1 and S2 positions, and we did not find any variation from the quadratic relation for the wavelength calibration.

Using the best-fit coefficients, we first converted the pixels along the dispersion direction to wavelength. We then determined the spectral plate scale as a function of wavelength, described as the number of wavelengths per unit pixel, which is shown in Figure 6 (right). We find a spectral plate scale of 10–14 mÅ in the key MaGIXS wavelength range from 10–17 Å.

To understand the deviation from linearity, we model the expected center pixel location along the image plane for the wavelength of the calibration lines and fitted the curve using standard grating equation, i.e.,

$$m\lambda = d(\sin \alpha - \sin \beta), \qquad (1)$$

where m is the diffraction order, λ is the wavelength of the calibration line, α is the normal incident angle, d is the line spacing at the center of grating, and β is the dispersion angle measured from the normal to the grating surface. We used α and the pixel offset as free model parameters. The best fit yields $\alpha = 88.3°$, which differs from the nominal optical design value of $88°$, and an offset of 76 pixels. While we recognize the deviation in the best-fit α, this could be interpreted from instrument buildup and alignment tolerances, which will be described in a future MaGIXS instrument and alignment paper (P. Champey et al. 2021, in preparation). The resulting fit is overplotted in Figure 6 (left) as a red line. The goodness of the

model fit is represented as the ratio between calibration wavelength and modeled wavelength, as shown in the bottom panel of Figure 6 (left). Hence, we confirm that the measured grating dispersion is consistent with the prescribed instrument design values.

4.3. Calibrated Spectral Image

Now that we have an established wavelength calibration, we then create a calibrated spectral image plot with the photon energy deposited plotted against the wavelength calibrated pixels. Figure 7 shows the spectral image plot constructed for targets Zn and Ni at the S0 beam position. Each dot in Figure 7 represents a photon of a particular wavelength appearing at appropriate pixel location abscissa on the detector. The energy of each photon event recovered from the algorithm is plotted in the ordinate. The location of first and second order lines, including the satellite lines, are highlighted appropriately in Figure 7. The solid lines are photon energy calculated from wavelength calibration for the first and second orders, respectively. It is evident the target emission lines from first and second orders are well pronounced in the spectral image and fall exactly on the respective calibrated solid lines. We also notice the distinct observation of first order oxygen peak from the target, which overlaps with the second order Zn lines; however, it could be well separated due to order sorting. All the other dots at high and low energies are continuum emission from the source. The target spectral lines appeared to have a spread in the recovered photon energy with an extended low-energy tail. We think this could be due to the detector's inherent complex spectral response owing to charge losses and/or limitation from event processing and therefore should be included while calculating the measured flux.

4.4. LSF

As MaGIXS is an imaging spectrograph instrument, the LSF could be envisaged as the PSF in the spectral direction. The LSF involves convolution of the telescope and spectrometer mirrors' performance, the grating's response, and the detector's spectral response. The combined response of the X-ray mirrors strongly depends on the figure quality of the mirrors, scattering on the mirror surfaces, and co-alignment of the TMA-SOA arrangement. The flatness, groove profile, and blaze angle
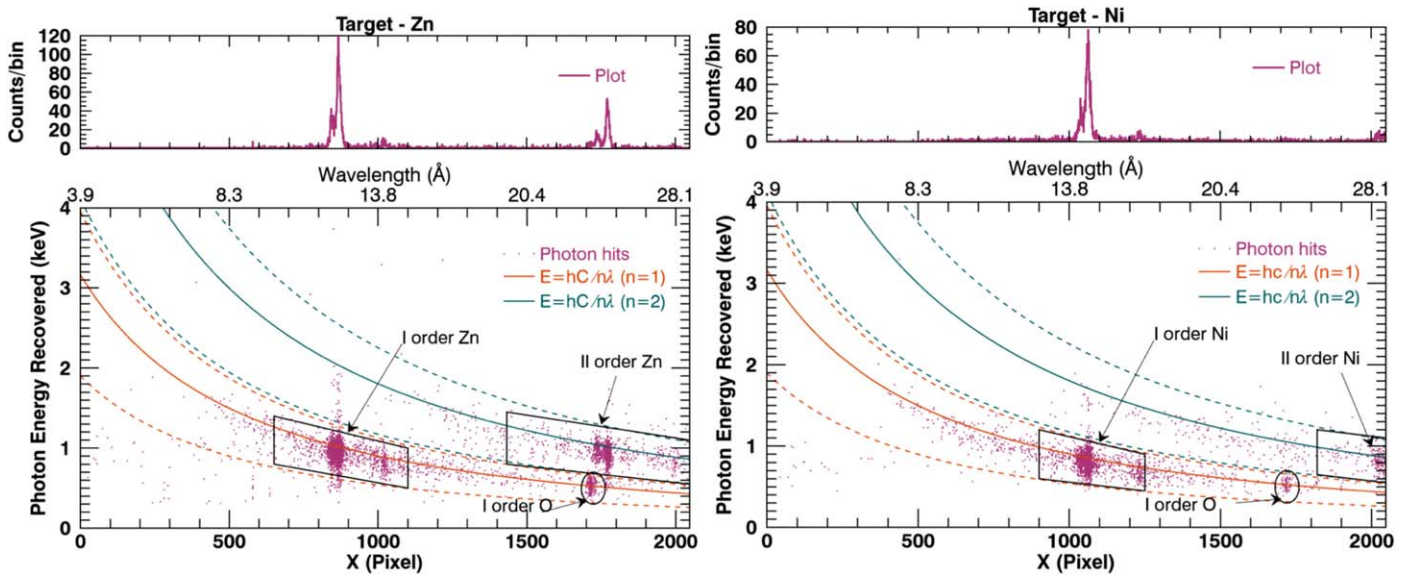
Figure 7. (Bottom panel) Calibrated MaGIXS grating produced spectral image plot constructed for target Zn (left) and Ni (right) at S0 beam position on the slot. Each dot represents a photon hit with dispersed wavelength in abscissa plotted against the respective energy deposited on the detector in ordinate. (Top panel) The resulting spectrum along the dispersion direction. Note that all of this spectral structure is unresolved by the BND, Figure 14. K-α and K-β lines of the respective targets are observed distinctly. The second order emission is very well observed within the detector pixels for target Zn; however, it is near the edge of the detector for target Ni.
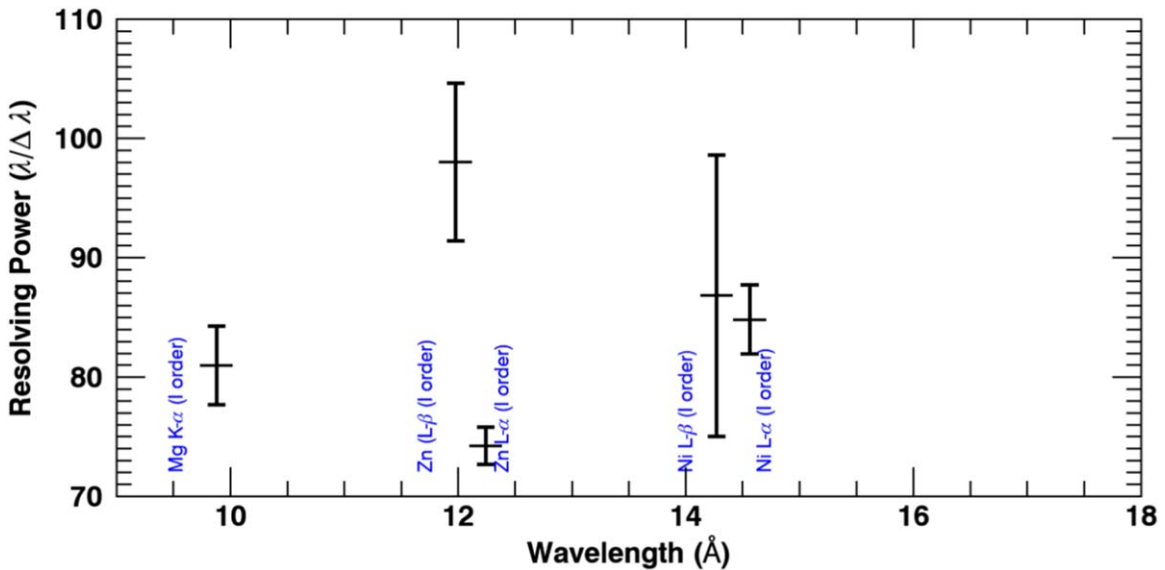
Figure 8. The resolving power of MaGIXS determined from the LSF of all imaged first-order lines.

determine the response of the grating. The LSF determines the overall spectral resolution of the instrument, which tells how well the instrument can separate two closely spaced emission lines. We modeled the first-order spectral lines with Gaussian functions and determined the FWHM (2.35 × σ) as a function of wavelength. Figure 8 shows the resolving power of MaGIXS defined by λ/FWHM($\delta\lambda$). The average spectral resolution of MaGIXS is ≈150 mÅ in the key MaGIXS wavelength range from 10–17 Å.
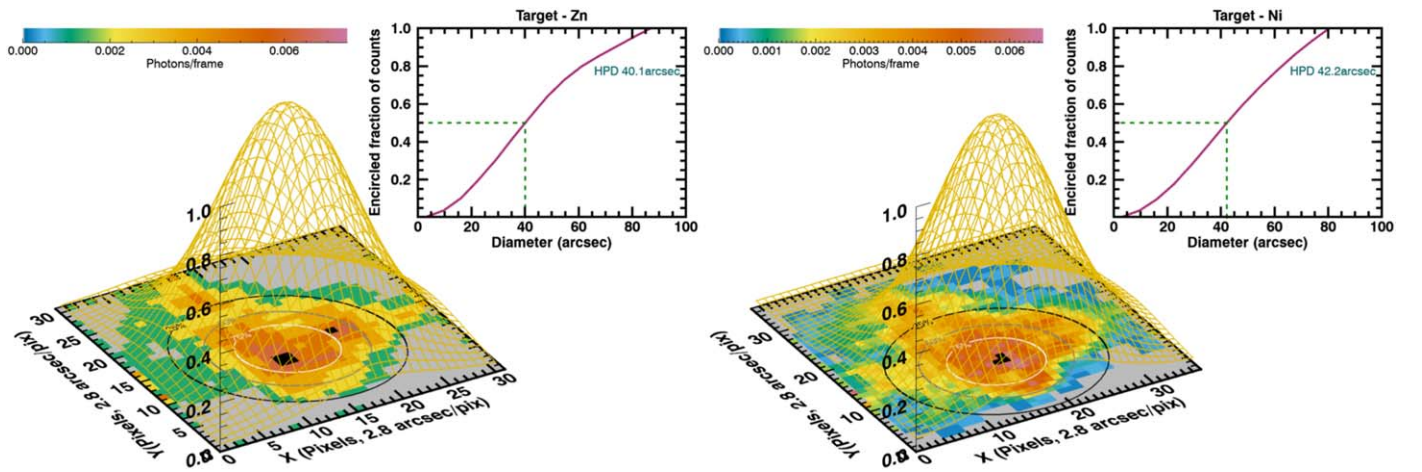
4.5. On-axis PSF

The PSF describes the instrument's ability to produce an image of a point source. For a PSF that follows the behavior of a Gaussian distribution, the width of the PSF determines the angular resolution of the instrument. Sources closer than this

value cannot be distinctly resolved. Another term for specifying the quality of the PSF is half-power diameter (HPD), or sometimes referred to as half-energy width—the diameter at which 50% of the detected power is encircled. These terms are useful for stating the resolving limit of imaging systems that produce PSF shapes that deviate from well-behaved Gaussian functions. Here, we use both Gaussian width and HPD to model and characterize the on-axis PSF produced by MaGIXS.

The X-ray performance of the individual MaGIXS mirrors showed a measurable improvement in the PSF of the active aperture (the sub-aperture dispersed by the grating), after a significant reduction of slope error was achieved using a computer numerical controlled (CNC) deterministic polishing technique on the mandrels (Champey et al. 2019; Davis et al. 2019). Champey et al. (2019) estimated the combined on-axis, full-aperture PSF using the on-axis image data from each of the

Figure 9. The measured on-axis PSF of MaGIXS for targets Zn (left) and Ni (right). The PSF images are smoothed with a 3 pixel width for better view. The ellipses demonstrate the action of the modeling the PSF using a 2D Gaussian, revealing the morphology. The ellipses shown here correspond to 30%, 50%, and 80% of the maximum intensity in the image. The bottom left panel shows the enclosed energy fraction of the on-axis PSF.

three individually tested mirrors comprising the TMA and SOA. However, the combined PSF of the small 34° aperture dispersed by the grating was omitted. Using the calibration data, we directly measured the combined on-axis PSF of MaGIXS. The resulting PSF includes the response of telescope mirror, spectrograph mirrors, the grating performance at different wavelengths, and both residual and gravity induced misalignment. We modeled the PSF using a two-dimensional Gaussian function as shown in Figure 9. The best-fit FWHM in the cross-dispersion direction is about $42''$–$47''$. Using the centroid determined from the best fit, we measured the HPD. The bottom left panel in Figure 9 shows the plot of encircled normalized counts as a function of circle diameter. In order to determine the cutoff radius for HPD calculation, we considered a conservative radius value at which the gradient in the encircled flux is less than 10%. From Figure 9, we measured the HPD of MaGIXS, shown by the purple dashed line, which is about $40''$–$45''$.

For cases where the PSF has a sharp core and narrow scattering wings, the curve tends to flatten quickly as the integral approaches the total integrated counts. However, our calibration experiments show that the PSF does not have a well-defined core, and the scattering wings are broad and diffuse. For this reason, the integrated count rate does not flatten quickly over the size of the evaluated frame. We hypothesize that this can be explained by the effects of the optics assemblies deflecting with respect to each other, under a 1G load. During the experiment, the instrument roll angle was positioned such that the cross-dispersion plane (Y-axis) was oriented parallel with the gravity vector. This would imply the influence of 1G deflection on the PSF would dominate in the cross-dispersion (Y) axis, which is consistent with the observed PSF shape. Dynamic and static analysis of the optical bench mechanical design indicated that a 1G environment causes a small, but significant amount of deflection between the TMA and SOA. We are continuing to investigate the source of this elongation of the spot in the Y (cross-dispersion) axis, and are applying the knowledge gained from our alignment measurements and mechanical analyses to the ray trace model, so that we can evaluate the influence of gravity induced misalignment on the PSF.

4.6. Radiometric Calibration

The aim of radiometric calibration for MaGIXS is to estimate the actual effective area of the end-to-end system. We can do this several ways: (1) theoretical calculations, (2) component level tests, and (3) end-to-end tests of the full system. In this section, we present the results from these three methods. The effective area is a wavelength-dependent quantity. Component and calibration tests provide measurements at discrete wavelengths only. We combine the theoretical and tests values to predict the effective area at all MaGIXS wavelengths. The results, summarized in Figure 10, show that both the end-to-end tests and the component level tests indicate the effective area of MaGIXS is reduced to roughly 20% of the theoretical value.

4.6.1. Theoretical Effective Area

The theoretical effective area (A_{eff}) of MaGIXS in flight configuration is defined by the following equation:

$$A_{\mathrm{eff}} = T_{\mathrm{Ent}} \times (A_{\mathrm{geo}} \times R_{\mathrm{primary}} \times R_{\mathrm{secondary}})$$
$$\times (R_{\mathrm{SM1}} \times R_{\mathrm{SM2}} \times G_{\mathrm{eff}}) \times T_{\mathrm{FP}} \times QE_{\mathrm{CCD}}, \quad (2)$$

where A_{geo} is the geometric effective aperture area in cm², T_{Ent} is the transmission of the entrance filter, R_{primary}, $R_{\mathrm{secondary}}$, R_{SM1}, and R_{SM2} are the reflectivities of two surfaces of the Wolter-I, SM1 and SM2 optics, G_{eff} is the measured first-order efficiency of grating (see Section 4.6.2), T_{FP} is the transmission of focal plane filter, and QE_{CCD} is the quantum efficiency of the CCD camera. All values in Equation (2) except the geometric area are unitless and reflect the percentage transmission (in the case of filters), reflection (in the case of optical elements), or detection (in the case of CCD). Except for the geometric area, all terms are functions of wavelength. In the test configuration, the entrance filter was not used, and the theoretical effective area calculated is shown in Figure 10 (solid black line). For the quantum efficiency of CCD (QE_{CCD}), we assumed the values of Hinode/XRT CCD. The reflectivity of X-ray mirrors including the TMA and the SM1-SM2 mirrors, and the X-ray transmission through window materials were calculated using the optical prescription values given in Table 1, following the
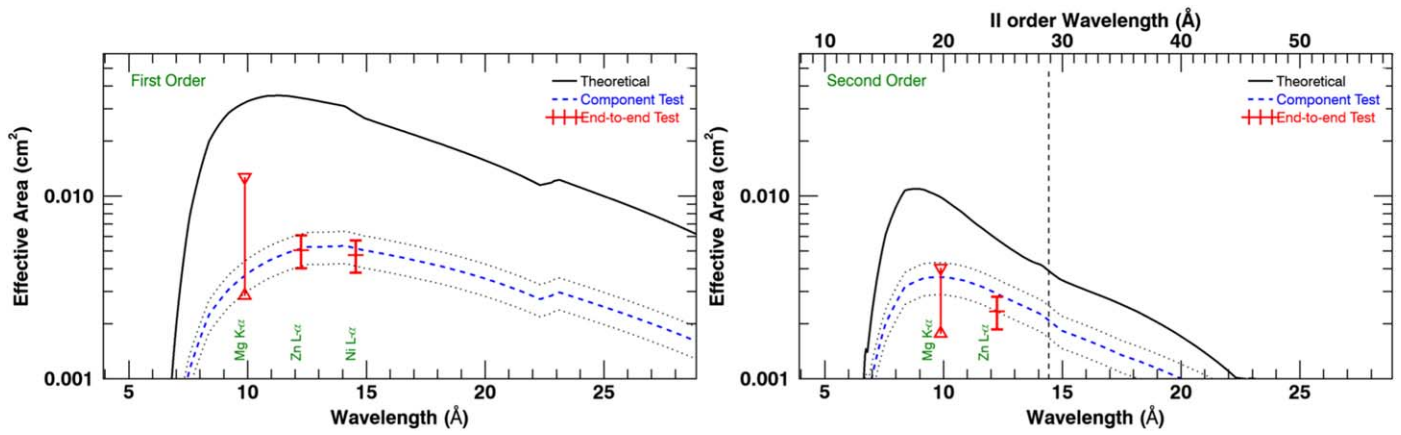
Figure 10. The effective area of MaGIXS instrument for the first (left) and second order (right), respectively. Only a portion of the second order spectrum falls on the detector. The vertical dashed line in the right panel denotes the wavelength corresponding to the last pixel on the detector. The solid black lines show the effective area calculated analytically using standard X-ray database values, excluding the entrance filter. The dashed blue lines represent the effective area updated with radiometric corrections calculated from component level testing, derived from the combined reduced reflectivity of the TMA and the SM1-SM2 mirrors, and measured grating efficiency. The first-order effective area derived from the component level tests is ∼4.5 times less than the theoretical values. The red points are the measured effective area at the characteristic X-ray wavelengths of the calibration targets Mg (9.88 Å), Zn (12.25 Å), and Ni (14.25 Å). The error bars are derived from the propagation of photon noise and the level of uncertainty in the incident X-ray flux. Due to additional noise in the Mg data, only meaningful upper and lower bounds are possible to determine. There is good agreement between the effective area derived from component level measurements and effective area from calibration tests.
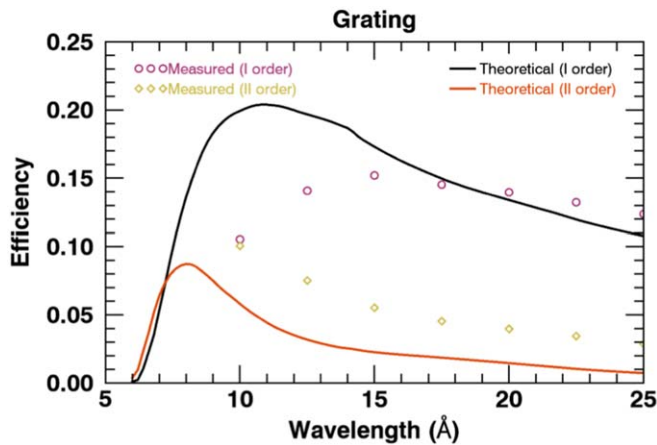
Figure 11. The first and second order theoretical efficiency of the grating measured are shown with solid black and red lines. The measured values of efficiency for the first order at different wavelengths are shown in circles, and the second order efficiency is shown in diamonds.

tabulated X-ray database values from Center for X-ray Optics https://henke.lbl.gov/optical_constants/. The theoretical efficiency of grating was calculated using PCGrate (Goray 2005) and the parameters listed in Table 1, are shown as solid lines in Figure 11. The first and second order theoretical effective areas calculated using the values described here are given in Figure 10 as black and red lines, respectively.

4.6.2. Component Level Testing

In this section, we discuss the component level testing that was completed on the optical components before integration (the grating) or during optical alignment (the TMA and SOA without the grating). There were no component level measurements of the focal plane filter or CCD, so we include their theoretical values when calculating the effective area.

Before integration into the SOA, the first and second order grating efficiency were measured using the Advanced Light Source beamline 6.3.2 at LBNL at seven wavelengths from

10–25 Å. The incident angle was fixed at 2° and the intensity of the diffracted orders was measured by scanning a detector. Measurements were performed at the center and ±25 mm from the center of the grating. The measured values are shown along with the theoretical values in Figure 11.

To evaluate the performance of telescope and spectrometer mirrors we analyzed X-ray test data collected during the assembly (S.Nos 1 and 2 in Table 2), when the full instrument was not yet built to compare the flux measured with the expected values. First, we assessed the reflectivity of the telescope mirror from data obtained during the TMA focus test, then we determined the reflectivity of the spectrometer mirrors during the TMA to SOA X-ray alignment confirmation. During this test, the grating was not installed. For all assembly tests, the Mg target was used at the source end with the respective filter with an optical depth of ∼2, which preferentially transmit the target's characteristic X-rays and suppresses the continuum. The BND data was processed as described in Paper I.

The presence of a filter at the X-ray source significantly suppressed the continuum emission, while retaining adequate line flux. The throughput of the TMA sub-aperture was measured by illuminating only the CNC-polished area and the CCD kept at the best focus position, where the slot was being placed. The CNC-polished region of the mirror could provide higher reflectivity, due to reduced slope errors in the parent mandrel fabrication. We performed photon counting on the CCD data using the event selection algorithm (see Paper I), and measured the TMA throughput flux. Figure 12 (left) shows an X-ray image of the TMA sub-aperture at the best focus position, the corresponding photon counting per event, and the X-ray spectrum to derive the measured X-ray flux are shown in Figure 12 (right). The expected throughput flux from the TMA sub-aperture is calculated by multiplying the theoretical reflectivity of the TMA (R_{TMA}) with the incident X-ray flux at the TMA entrance derived from BND spectral analysis. The ratio of the measured and expected TMA flux is determined to be 0.4, which is the correction factor required for radiometric TMA reflectivity. This offset implies that the throughput of the TMA reduces the intensity of the incident beam by about 60%.
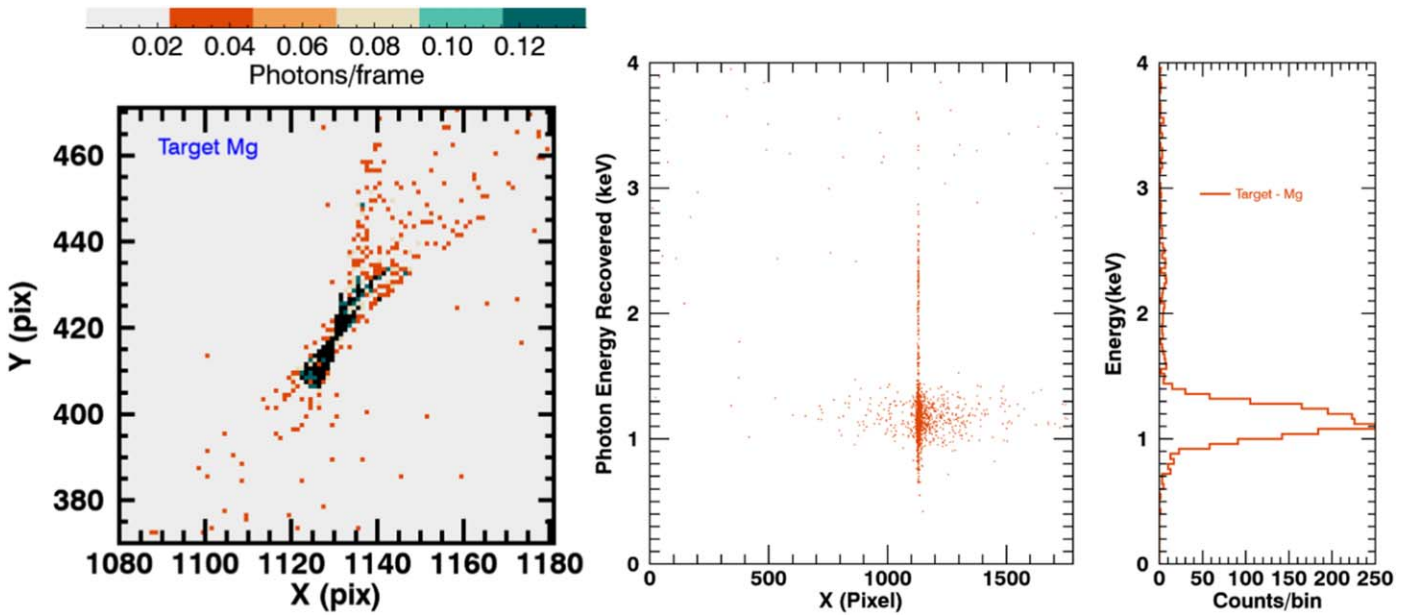
Figure 12. (left) X-ray image of the TMA sub-aperture at the best focus position. (Right) X-ray spectral image with photon energy plotted as a function of pixel location in the *X*-direction. The histogram of the binned energy spectrum shows the strong Mg K-α line in the subpanel.
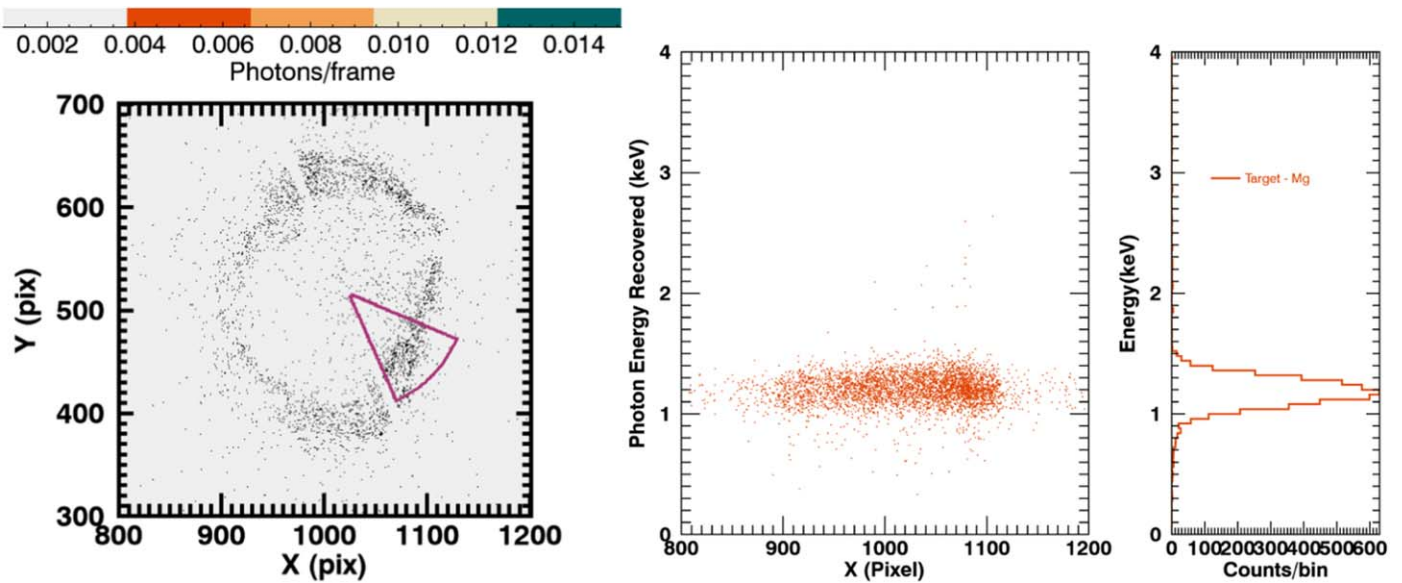

Figure 13. (Left) Full-aperture X-ray image of the co-aligned TMA-SM1-SM2 configuration at an out-of-focus distance. X-ray photons coming from the CNC-polished area is highlighted. (Right) X-ray spectral image of the full-aperture with photon energy plotted as a function of pixel location in the *X*-direction. The histogram of the binned energy spectrum shows the strong Mg K-α line in the subpanel.

We then assessed the combined radiometry of spectrometer mirrors (SM1 and SM2) using an assembly test data repository with a co-aligned TMA and SM1-SM2 mirror configuration at an out-of-focus position. Figure 13 shows the X-ray image of the TMA-SM1-SM2 data with the good portion of the image highlighted. The expected throughput from the TMA-SM1-SM2 configuration is calculated by multiplying the incident X-ray flux at the TMA entrance derived from BND spectral analysis with the theoretical reflectivity of the TMA, TMA correction factor (0.4), and theoretical reflectivity of SM1 and SM2. The ratio of measured and expected flux gives the correction factor required for the combined SM1-SM2 reflectivity, which is found to be

0.54. This offset implies that the spectrometer mirrors further reduce the intensity by about 46%.

Therefore, the overall radiometric correction factor for the combined reflectivity of the TMA and SM1-SM2 mirrors is $\sim$0.216, which means that the throughput flux reaching the grating would be $\sim$20% of the incident X-ray flux. Using component level calibration tests, we revise the theoretical effective area curve for the first and second orders by including the measured grating efficiency and multiplying the optics reflectivities by the correction factors, which is shown as the blue dashed line in Figure 10. Though the correction factors were taken at a single wavelength, we assumed the correction
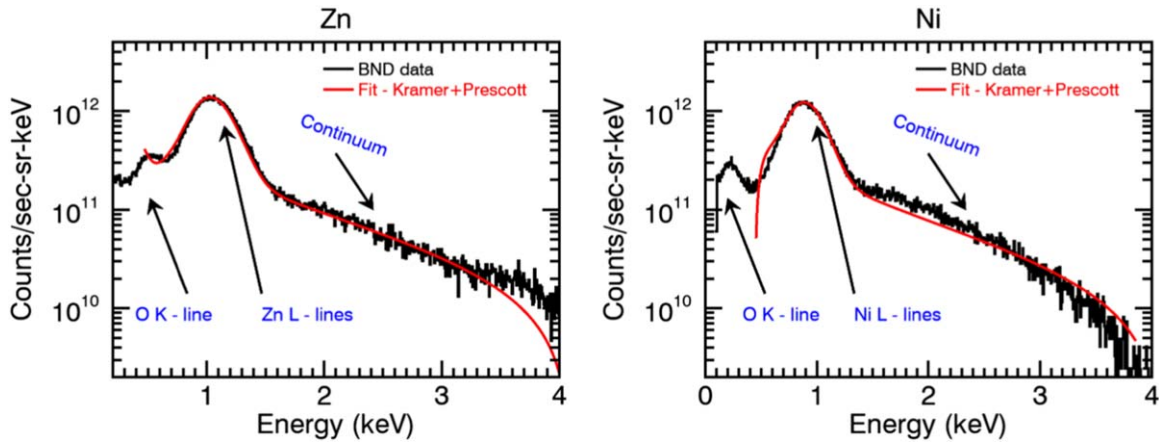
Figure 14. The unfiltered incident X-ray spectra from targets Zn and Ni as measured by the BND. The continuum and target line emission are modeled using Kramer's function and the Prescott function and the corresponding line intensities are determined. We acknowledge the presence of an O emission line in the observed BND spectra; however, it is not included in the spectral modeling.

factor applies to the entire wavelength range when calculating component level effective area.

4.6.3. Measured Effective Area

We first calculate the expected incident line flux at the MaGIXS aperture through spectral analysis of BND data, which is slightly different from Paper I, as there was no filter at the source end for all targets during calibration tests because we had the MaGIXS focal plane filter installed in front of the CCD. Therefore, the observed BND spectra include photons from source lines plus a strong continuum at relatively poor energy resolution. However, MaGIXS observed a dispersed spectra with much higher spectral/energy resolution, where we can separate the continuum and the source lines. Because the MaGIXS response varies significantly over wavelength and the goal of this exercise is to measure the effective areas at discrete wavelengths, we modeled the source line and continuum in the BND data with a Prescott function (Prescott 1963) and Kramer's equation. We mention that the flux derived under the line would also have some continuum contribution ($<10\%$). Apart from the source line, we also observed a low-energy oxygen line in the BND data; however, we did not include spectral modeling to avoid complex spectral response deconvolution of the BND, which is beyond the scope of this work. For spectral analysis and flux estimates, we used the quantum efficiency of the BND (Weisskopf & O'Dell 1997). Sample spectral fits to BND data with models for line and continuum emission are shown in Figure 14.

The total number of photons reaching the MaGIXS science camera after dispersion from the grating is determined from the calibrated spectral image shown in Figure 7. We count the total number of photons within a tolerance energy level considering a range of pixels encompassing all the target lines, including satellite lines. For instance, with the Zn target, we count all detected photons that fall between ∼600 and 1100 pixels and have a tolerance energy range of E_{ph} −35% to E_{ph} +25% E_{ph} as a detected Zn photon, where E_{ph} is the photon energy. The tolerance levels are marked as dashed lines in Figure 7. The reason for the larger tolerance (−35%) on the lower wavelength side is to accommodate the low-energy tail photons. In addition, we also observe a small fraction of pileup photons with energy deposits greater than target line energies, appearing at the respective target's first-order pixel

wavelengths. We include these photons in our flux estimates by counting them twice. We divide the number of detected photons by the total observation time to get the photons per seconds in the MaGIXS science camera. We then calculate the effective area of MaGIXS at the target's line energy by taking the ratio of this to the expected flux determined from the BND analysis. This method works well for the data from the Zn and Ni targets.

As mentioned in Section 3, the Mg data suffered from additional noise due to the cooling system pausing and the detector warming during data collection. The noise floor of the data increased over time and *hot pixels* increased intensity over time. These hot pixels masquerade as photon hits and can significantly impact flux estimates. We identified columns of hot pixels and determined meaningful upper and lower flux limits, which are shown as triangles in Figure 10, by including and excluding them in photon counting.

4.6.4. Results of Radiometric Calibration

Figure 10 shows the effective area curve of MaGIXS for the first order (left) and second order (right). We mention that only a portion of the second order spectrum falls on the detector, which would result in a systematic underestimation of flux from the measurement data. The solid black lines denote the effective area calculated analytically using standard X-ray database values excluding the entrance filter using the optical prescription values given in Table 1. The estimated effective area derived from the component level tests is shown by the dashed blue lines. This value includes measured grating efficiency (Figure 11) and the correction factors derived for the reflectivity of the TMA and the SM1-SM2 mirrors measured at a single wavelength, which was then applied to the entire wave band. The measured effective area at discrete wavelengths from the calibration tests are overplotted with error bars. The error bars are calculated by propagating errors in the measured MaGIXS flux, which is statistical Poisson noise and a conservative 20% error for the expected incident flux determined from Paper I, which dictates the final error in the measured effective area. Due to the additional noise in Mg data (see Section 3), we have derived meaningful upper and lower limits for the effective area, denoted by the triangles. We also applied a conservative error estimate of 20% to the effective area derived from the component level tests, showing
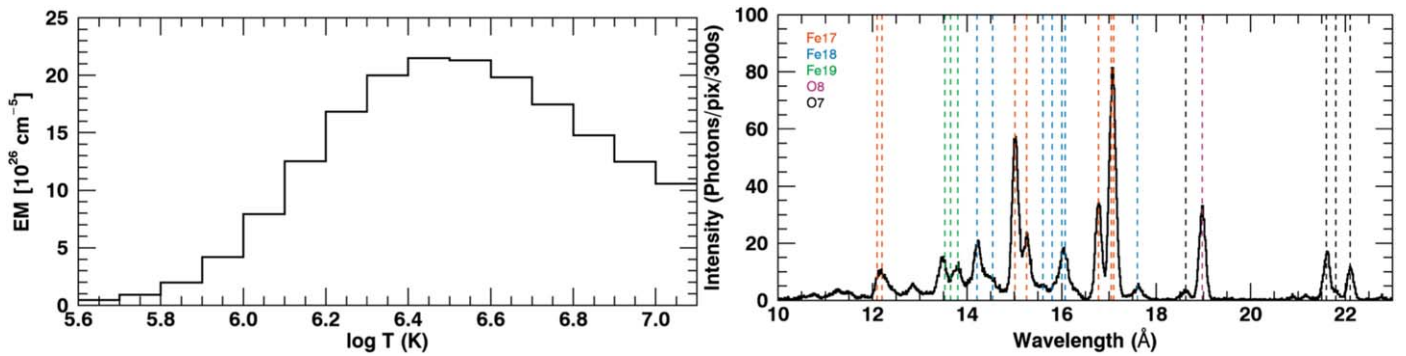
Figure 15. (Left) The EM distribution of a typical solar active region taken from the Chianti atomic database, used to predict in flight MaGIXS expected intensity. (Right) The predicted MaGIXS spectrum for a typical solar active region. The dashed vertical lines indicate some of the strong lines of Fe XVII, Fe XVIII, and Fe XIX that MaGIXS will observe. This spectrum includes an instrumental broadening of FHWM = 0.15 Å, which is the measured average LSF of MaGIXS.

the upper and lower bounds for the deduced effective area curve, represented by dotted lines in Figure 10. The measured effective area is ∼4.5 times less than the theoretical radiometric prediction. The effective area curve derived from the component level tests using correction factors for the reflectivity of the mirrors and the measured grating efficiency closely agree with the measured effective area values at discrete wavelengths (see Table 6).

5. Prediction of Count Rates for MaGIXS Flight

We use the measured instrument response, including the wavelength calibration and effective area, to calculate the expected MaGIXS intensity during flight observing a typical solar active region. To obtain the line intensities, we used EM distribution corresponding to a typical solar active region taken as available in the CHIANTI v.9 database, as shown in Figure 15 (left). Figure 15 (right) shows an example of the predicted MaGIXS spectrum, which is obtained by folding the MaGIXS response through the EM distribution shown in Figure 15 (left). Table 5 gives some of the strong emission lines in the MaGIXS wavelength range for different ion species, the maximum temperature of emission, and the expected signal strength in units of photons pixel^{-1} 300 s^{-1} integrated over spectral lines from first and second orders, for the entire flight duration. We note that these EM estimates are approximate and are derived based on available space instrumentation, which has a blindspot for the high-temperature EM slope as demonstrated in Winebarger et al. (2012) and Athiray et al. (2019). We notice the strongest and brightest lines are Fe XVII 17.07, 16.78, and 15.01 Å, and O VII 21.60 and 22.10 Å, and O VIII 18.97 Å, but there are lines from Fe XVIII 14.54, 14.21, 15.83, 16.00, and 16.07 Å, and Fe XIX 13.53 Å in the MaGIXS wavelength range. These lines provide the expected temperature sensitivity of MaGIXS covering warm and hot plasma emission. We notice that for the simulated typical active region EM distribution, the predicted count rates for the diagnostic Fe XVIII and Fe XIX are low and therefore several pixels may need to be summed to achieve adequate counts in those emission lines.

6. Summary and Discussion

In this paper, we have presented our analysis and results of MaGIXS end-to-end instrument calibration using the 500 m X-ray beam at XRCF at NASA MSFC. The measurements are carried out using X-ray beams from three different targets viz

Table 5
Predicted MaGIXS Flux for Some of the Strong Emission Lines in the MaGIXS Wavelength Range

Ion	Wavelength	Log Maximum Temperature	Predicted MaGIXS Flux First Order Photons pixel^{-1} 300 s^{-1}	Predicted MaGIXS Flux Second Order Photons pixel^{-1} 300 s^{-1}
	Å			
O VII	22.10 Å	6.30	401	…
O VII	21.60 Å	6.30	661	…
O VIII	18.97 Å	6.40	847	…
Fe XVIII	17.62 Å	6.80	18	…
Fe XVII	17.07 Å	6.60	677	…
Fe XVII	16.78 Å	6.60	275	…
Fe XVIII	16.07 Å	6.80	37	…
Fe XVIII	16.00 Å	6.80	24	…
Fe XVIII	15.83 Å	6.80	14	…
Fe XVII	15.26 Å	6.60	125	…
Fe XVII	15.01 Å	6.60	432	…
Fe XVIII	14.54 Å	6.80	14	…
Fe XVIII	14.21 Å	6.80	45	…
Fe XIX	13.53 Å	6.95	23	…
Fe XVII	12.2 Å	6.95	80	52
Fe XVII	11.2 Å	6.80	15	11
Mg XI	9.3 Å	6.80	10	11
Mg XI	9.2 Å	6.80	15	18

Mg, Zn, and Ni. Calibration data are analyzed using the photon counting method published in Paper I, to measure photon energy and flux. We have performed wavelength calibration using eight wavelengths arising from the first and second order grating diffraction of the three selected target emission lines. The summary of MaGIXS calibration parameters is given in Table 6. We find that pixel to wavelength calibration can be well modeled using a quadratic function, as shown in Figure 6. The measured dispersion in the key wavelength range i.e., from 10–17 Å is found to be 10–15 mÅ. Using photon counting, we then created calibrated spectral images with the wavelength calibrated pixels plotted against the photon energy deposited on the pixels, as shown in Figure 7. Using these plots, we highlighted the significance of photon counting to identify emission at different wavelengths, including the capability to delineate the overlap of different first and second order emission lines. We observed a close match between the photon energy derived from the wavelength calibration and the photon
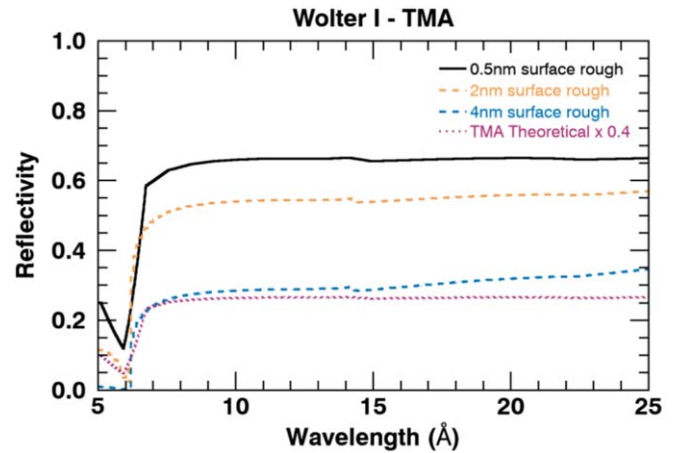
Table 6
MaGIXS Calibration Parameters

Parameter	Value
Pixel-to-wavelength calibration coefficients	2.231×10^{-6} (second order term)
	0.00763 (first order term)
	3.93 (offset)
Average spectral plate scale (10–17 Å)	11 mÅ
Average LSF	∼150 mÅ in 10–17 Å
Effective area (cm²)	0.0050 at 12.25 Å
	0.0047 at 14.55 Å
PSF	40–45″ HPD

Figure 16. Reflectivity of the TMA Wolter-I type mirror, including primary and secondary, for different surface roughness values. Solid curve represents reflectivity for the mirror prescription given in Table 1. Surface roughness of ≈4 nm (dashed line); an extreme case is required if it were to explain the reduced TMA reflectivity (dotted line).

energy deposited on the detector. Furthermore, we performed spectral line fits to the calibration data along the dispersion direction and determined the LSF to be ≈150 mÅ.

Using the simultaneous measurement of incident X-ray spectra with a BND, we measured the effective area of the MaGIXS instrument, which is ≈4.5× less than the theoretical effective area calculated from standard X-ray database values for the mirrors, filter transmission, and grating efficiency. In addition, we also analyzed X-ray data from the assembly tests with the aligned TMA and TMA-SM1-SM2 configuration and evaluated the radiometric throughput of telescope and spectrometer mirrors. We find a correction factor of 0.4 to the TMA reflectivity and 0.54 for the combined reflectivity of SM1 and SM2. The combined radiometric correction factor for the throughput from the telescope and spectrometer mirrors is 0.216, which closely agrees with the measured MaGIXS effective area from the calibration tests. This offset implies a reduction of about 80% in effective area from the theoretical values, most of that reduction coming from the telescope and spectrometer mirrors. From our understanding of the instrument and experimental setup, there could be many reasons why we see an overall reduced throughput from these mirrors. However, it is not trivial to quantify these factors. Here, we list some of the major factors of which some combination could be responsible for the overall reduction in the throughput.

1. Surface roughness of telescope and spectrometer mirrors: MaGIXS mirrors are produced using and electroforming replication process, pioneered at MSFC—the same process used in High-Energy Replicated Optics, the Astronomical Roentgen Telescope X-ray Concentrator, Focusing Optics X-ray Imager, and Imaging X-Ray Polarimetry Explorer. The prescribed surface roughness of the X-ray mirrors is ⩽5 Å. At this point, the mandrels used for replicating MaGIXS mirrors are fabricated using the state-of-the-art CNC polishing technique. The surface profile of the CNC-polished mandrels mapped using metrology showed a significant reduction in slope errors and the estimated HPD ranges from ≈ 3.5″–7″. However, an important caveat is that there is no direct way to measure the surface profile of the replicated mirror shells. The X-ray performance evaluation of these mirrors showed only a marginal improvement in the HPD. Historically, the replication errors are expected to degrade the performance by a factor of 2, which sets an approximate upper limit of 10 Å for the surface roughness. The theoretical reflectivity of the TMA Wolter-I

mirror calculated using standard X-ray database values for the optical prescription given in Table 1, as shown in Figure 16 and represented by the solid line. Keeping the optical prescription the same, we vary the surface roughness of the mirror until the TMA reflectivity is ≈40% of the original values, plotted as the sequence of dotted lines in Figure 16. The plot indicates that a surface roughness of ≈4 nm is required if that is to solely account for the reduced reflectivity. This is an extreme case and is not supported by the measured on-axis optical performances. Therefore, the real surface roughness of the mirrors, which we cannot directly measure at this point, likely lies somewhere between these two bounds.

2. Vignetting and alignment errors: In general, X-ray mirrors in a telescope are optimized around the optical axis, where the effective area is maximum. An increase in off-axis angle of the mirrors would worsen the PSF, and also affect the throughput flux. This situation is generally known as vignetting, which is defined as the ratio between the measured source intensity imaged at a given position and the measured intensity of the same source aligned to the optical axis. For MaGIXS, where the X-ray mirrors are arranged in series followed by the grating, the relative co-alignment of the TMA, spectrometer mirrors, and grating with respect to the optical axis is critical. The assemblies (TMA, SOA) are co-aligned on the optical bench using a theodolite up to the mechanical tolerance levels. However, when there is an offset of the optical center from the geometrical center of any of the mirror, it results in vignetting, which is very challenging and complicated to experimentally measure and quantify. We have performed experiments to assess if there is any possible vignetting by the top-hat structure that supports the entrance filter of the TMA, through X-ray measurements with and without a top hat, which did not reveal any significant change in the TMA throughput. However, these results are difficult to interpret as they were conducted on different dates, and in between, some changes were made to the setup. The contribution from vignetting is not fully addressed in this first MaGIXS rocket flight calibration, and a more thorough

investigation will be carried out for future flights. We emphasize that this will not significantly affect MaGIXS science observations as we have measured the effective area.

3. Grating efficiency: The measured first-order grating efficiency is less than the theoretical prediction for low wavelengths below ∼15 Å (see Figure 11), while the second order overperforms by ∼100% at all measured wavelengths. We also notice a difference in the shape of the efficiency curve between the theory and measurement. These observations could be explained by an imperfect blaze angle in the grating. For instance, an increase in blaze angle from the nominal value would shift the peak of the efficiency curve to longer wavelengths in both first and second orders, respectively. This change in blaze angle would also reduce the first-order efficiency considerably, while increasing the second order efficiency, as seen in the measurement. In addition, the manufacturing and coating process of the grating left residual material at the edge of each saw tooth, which could also impact the measured efficiency. A more detailed investigation of grating performance, including modeling efforts, will be presented in a future paper and is beyond the scope of the work described here.

4. Assumption of CCD efficiency: We assumed the efficiency values of the Hinode/XRT CCD in our analysis, which is a reasonable approximation given that the MaGIXS CCD is an astro-processed, back-illuminated CCD from e2V Technologies Ltd. In Athiray et al. (2019), we used a similar flight grade astro-processed CCD from e2V Technologies Ltd., which yields close agreement with the BND results. Moody et al. (2017) showed that the astro-processed CCDs from e2V Technologies Ltd. have been demonstrated to be reliable and consistent in the MaGIXS energy range. Therefore, we conclude that although we have not directly measured the quantum efficiency of the MaGIXS flight camera, we believe that it will not have a significant impact on explaining the observed throughput of MaGIXS.

Using the measured MaGIXS calibration products, such as wavelength calibration, instrument broadening (FWHM), and the updated effective area, we predicted expected line fluxes for a typical active region observation during a MaGIXS flight. However, we note that the EM used in our forward model is an approximation derived from the existing instruments, which cannot precisely quantify high-temperature emission. Our results presented here suggest that observing a bright/hot active region during a MaGIXS flight would be highly beneficial to maximize science throughput.

ORCID iDs

P. S. Athiray ⓘ https://orcid.org/0000-0002-4454-147X
Amy R. Winebarger ⓘ https://orcid.org/0000-0002-5608-531X
Patrick Champey ⓘ https://orcid.org/0000-0002-7139-6191
Ken Kobayashi ⓘ https://orcid.org/0000-0003-1057-7113
Sabrina Savage ⓘ https://orcid.org/0000-0002-6172-0517
Alexander R. Bruccoleri ⓘ https://orcid.org/0000-0001-5927-3300
Leon Golub ⓘ https://orcid.org/0000-0001-9638-3082
Ralf K. Heilmann ⓘ https://orcid.org/0000-0001-9980-5295
Chad Madsen ⓘ https://orcid.org/0000-0001-8775-913X
Mark L. Schattenburg ⓘ https://orcid.org/0000-0001-6932-2612
Genevieve D. Vigil ⓘ https://orcid.org/0000-0002-7219-1526

References

Asgari-Targhi, M., & van Ballegooijen, A. A. 2012, ApJ, 746, 81
Athiray, P. S., Winebarger, A. R., Barnes, W. T., et al. 2019, ApJ, 884, 24
Athiray, P. S., Winebarger, A. R., Champey, P., et al. 2020, ApJ, 905, 66
Barnes, W. T., Bradshaw, S. J., & Viall, N. M. 2019, ApJ, 880, 56
Barnes, W. T., Cargill, P. J., & Bradshaw, S. J. 2016a, ApJ, 829, 31
Barnes, W. T., Cargill, P. J., & Bradshaw, S. J. 2016b, ApJ, 833, 217
Cargill, P. J., Mariska, J. T., & Antiochos, S. K. 1995, ApJ, 439, 1034
Champey, P., Athiray, P. S., Winebarger, A. R., et al. 2019, Proc. SPIE, 11119, 1111917
Champey, P., Kobayashi, K., Winebarger, A., et al. 2015, Proc. SPIE, 9601, 208
Champey, P., Winebarger, A., Kobayashi, K., et al. 2016, Proc. SPIE, 9905, 990573
Cranmer, S. R., & Winebarger, A. R. 2019, ARA&A, 57, 157
Davis, J., Champey, P., Kolodziejczak, J., & Griffith, C. 2019, Proc. SPIE, 11119, 260
Goray, L. 2005, NIMPA, 536, 211
Hertz, E., Cheimets, P., Hohl, J., et al. 2020, Proc. SPIE, 11444, 1212
Klimchuk, J. A. 2006, SoPh, 234, 41
Klimchuk, J. A. 2017, arXiv:1709.07320
Kobayashi, K., Cirtain, J., Golub, L., et al. 2010, Proc. SPIE, 289, 4393
Kobayashi, K., Cirtain, J., Winebarger, A. R., et al. 2014, SoPh
Kobayashi, K., Winebarger, A. R., Savage, S., et al. 2018, Proc. SPIE, 10699, 1069927
Moody, I., Watkins, M., Bell, R., et al. 2017, CCD QE in the Soft X-ray Range, e2v Technologies, Open Univ, http://oro.open.ac.uk/49003/
Parker, E. N. 1988, ApJ, 330, 474
Prescott, J. R. 1963, NucIM, 22, 256
Rachmeler, L. A., Winebarger, A. R., Savage, S. L., et al. 2019, SoPh, 294, 174
Reep, J. W., Bradshaw, S. J., & Klimchuk, J. A. 2013, ApJ, 764, 193
Wargelin, B. J., Kellogg, E. M., McDermott, W. C., Evans, I. N., & Vitek, S. A. 1997, Proc. SPIE, 3113, 526
Warren, H. P., Winebarger, A. R., & Brooks, D. H. 2012, ApJ, 759, 141
Weisskopf, M. C., & O'Dell, S. L. 1997, Proc. SPIE, 3113, 2
Winebarger, A. R., Warren, H. P., Schmelz, J. T., et al. 2012, ApJL, 746, L17
Winebarger, A. R., Weber, M., Bethge, C., et al. 2019, ApJ, 882, 12